

# Polar patterns of driven filaments

Volker Schaller<sup>1</sup>, Christoph Weber<sup>2</sup>, Christine Semmrich<sup>1</sup>, Erwin Frey<sup>2</sup> & Andreas R. Bausch<sup>1</sup>

The emergence of collective motion exhibited by systems ranging from flocks of animals to self-propelled microorganisms to the cytoskeleton is a ubiquitous and fascinating self-organization phenomenon<sup>1–12</sup>. Similarities between these systems, such as the inherent polarity of the constituents, a density-dependent transition to ordered phases or the existence of very large density fluctuations<sup>13–16</sup>, suggest universal principles underlying pattern formation. This idea is followed by theoretical models at all levels of description: micro- or mesoscopic models directly map local forces and interactions using only a few, preferably simple, interaction rules<sup>12,17–21</sup>, and more macroscopic approaches in the hydrodynamic limit rely on the systems' generic symmetries<sup>8,22,23</sup>. All these models characteristically have a broad parameter space with a manifold of possible patterns, most of which have not yet been experimentally verified. The complexity of interactions and the limited parameter control of existing experimental systems are major obstacles to our understanding of the underlying ordering principles<sup>13</sup>. Here we demonstrate the emergence of collective motion in a high-density motility assay that consists of highly concentrated actin filaments propelled by immobilized molecular motors in a planar geometry. Above a critical density, the filaments self-organize to form coherently moving structures with persistent density modulations, such as clusters, swirls and interconnected bands. These polar nematic structures are long lived and can span length scales orders of magnitudes larger than their constituents. Our experimental approach, which offers control of all relevant system parameters, complemented by agent-based simulations, allows backtracking of the assembly and disassembly pathways to the underlying local interactions. We identify weak and local alignment interactions to be essential for the observed formation of patterns and their dynamics. The presented minimal polar-pattern-forming system may thus provide new insight into emerging order in the broad class of active fluids<sup>8,23,24</sup> and self-propelled particles<sup>17,25</sup>.

The molecular system that we consider consists of only a few components: actin filaments and fluorescently labelled reporter filaments that are propelled by non-processive motor proteins (heavy meromyosin (HMM)) in the planar geometry of a standard motility assay<sup>26</sup> (Fig. 1). The molecular nature of this approach permits large system sizes and possibly high particle densities with only a few, easily adjustable key parameters. To investigate the stability and dynamics of collective phenomena, the filament density,  $\rho$ , is chosen as control parameter and is systematically varied.

Depending on  $\rho$ , two phases are discernable: a disordered phase below a critical density,  $\rho_c$ , of  $\sim 5$  filaments per square micrometre, and an ordered phase above  $\rho_c$ . In the disordered phase at low actin concentrations, the filaments, with a length of about  $10\ \mu\text{m}$ , perform persistent random walks without any specific directional preference. Their speed ( $v_0 = 4.8 \pm 0.5\ \mu\text{m s}^{-1}$ ) is set by the motor proteins at the surface and the adenosine tri-phosphate (ATP) concentration ( $c_{\text{ATP}} = 4\ \text{mM}$ ). The observed directional randomness is thermal in

nature but also reflects the motor distribution and activity at the surface<sup>27</sup>.

Increasing the filament density above  $\rho_c$  results in a transition to an ordered phase that is characterized by a polymorphism of different polar nematic patterns coherently moving at the speed  $v_0$  (Fig. 2). These patterns can be further classified according to their size, orientational persistence, overall lifetime and assembly/disassembly mechanisms: in an intermediate-density regime above  $\rho_c$ , moving clusters (swarms) of filaments appear; in the high-density regime, starting at a threshold density of  $\rho^*$  ( $\sim 20$  filaments per square micrometre), propagating waves start to form. Both patterns are characterized by persistent density modulations.

The clusters encountered in the intermediate state move independently and have cluster sizes ranging from about  $20\ \mu\text{m}$  to more than  $500\ \mu\text{m}$  in diameter (Fig. 2a, b). In general, clusters have an erratic motion with frequent reorientations of low directional persistence (Fig. 2a, b and Supplementary Movie 1). The low orientational persistence affects the cluster's shape but barely influences its temporal stability. The cluster integrity is only affected if collisions with boundaries or other clusters are encountered. Increasing the filament density in this intermediate regime not only yields larger clusters but also a more persistent cluster movement. Individual clusters spontaneously emerge from the dilute, disordered background and

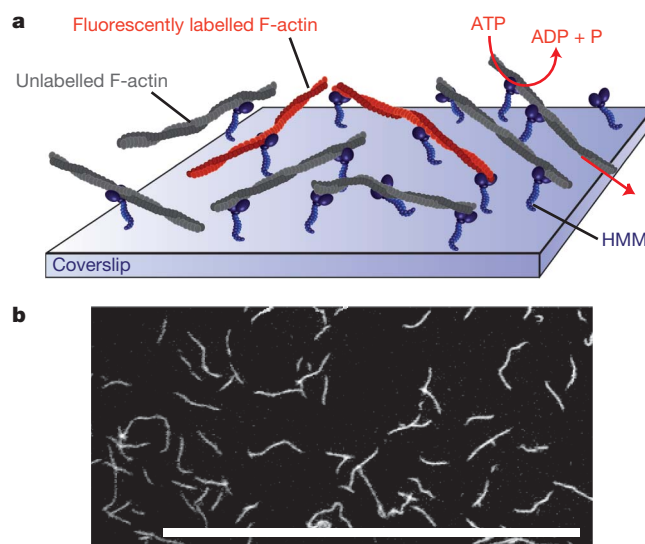


**Figure 1 | Schematic of the high-density motility assay.** **a**, The molecular motor HMM is immobilized on a coverslip and the filament motion is visualized by the use of fluorescently labelled reporter filaments with a ratio of labelled to unlabelled filaments of  $\sim 1:200$  to  $1:320$ . **b**, For low filament densities, a disordered phase is found. The individual filaments perform persistent random walks without any specific directional preferences. Encounters between filaments lead to crossing events with only slight reorientations. Scale bar,  $50\ \mu\text{m}$ .

<sup>1</sup>Lehrstuhl für Biophysik-E27, Technische Universität München, 85748 Garching, Germany. <sup>2</sup>Arnold Sommerfeld Center for Theoretical Physics and CeNS, Department of Physics, Ludwig-Maximilians-Universität München, 80333 Munich, Germany.

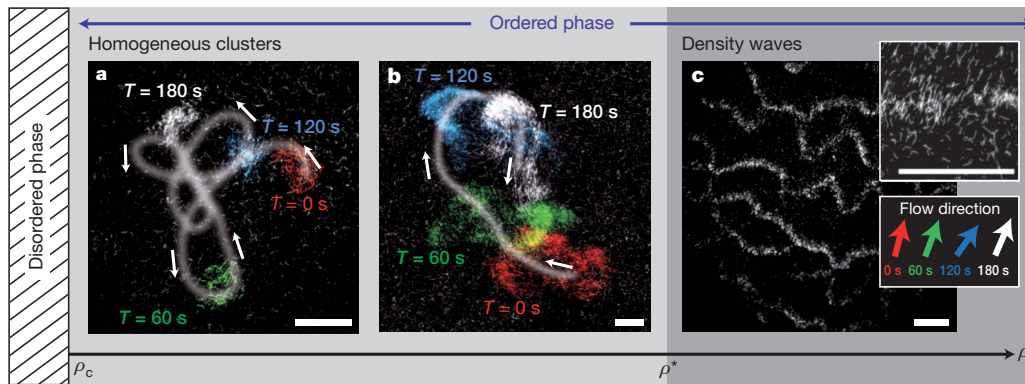


**Figure 2 | Phase behaviour as a function of the filament density.** For low densities, a disordered phase is found. Above a certain critical density,  $\rho_c$ , in an intermediate-density regime, the disordered phase is unstable and small polar nematic clusters of coherently moving filaments start to form (a; Supplementary Movie 1). At higher densities, these clusters become larger but remain homogeneous (b). Above a threshold density,  $\rho^*$ , in the high-density regime, persistent density fluctuations lead to the formation of wave-like structures (c; Supplementary Movie 2). In addition, an enhanced

continuously lose and recruit filaments. As long as single clusters are embedded in this homogeneous disordered background while they move, this uptake and loss dynamics is balanced and leads to cluster sizes that are stable for several minutes.

A further increase of filament concentration above  $\rho^*$  results in density waves characterized by correlated movement of high-density regions. In this high-density regime, the filaments move predominantly in bands that are stable throughout the observation time (up to 30 min). The bands exceed the size of their constituents by up to three orders of magnitude, almost spanning the entire system and forming crescent-shaped substructures. The appearance of the bands is a generic feature of the high-density motility assay. Whereas filaments in the high-density regions move collectively with high orientational persistence, filaments lying outside the bands perform persistent random walks (Fig. 2c and Supplementary Movie 2). The system is less sensitive to other control parameters, such as the ATP concentration or the filament length.

In all states above  $\rho_c$ , swirls or spirals of actin filaments can also be observed, reminiscent of spiralling patterns predicted by active gel theory<sup>23</sup>. They form spontaneously either from the random movement

directional persistence is observed with increasing filament density. In a and b, the trajectory of the clusters is shown by a colour-coded time overlay of their movements in time (white line). The movement of the small cluster in a has a low persistence length,  $L_p \approx 65 \mu\text{m}$ . The cluster in b is larger, less prone to reorientations and has a considerably higher persistence length ( $L_p \approx 200 \mu\text{m}$ ). The insets in c show a magnified view and a local analysis of the average flow direction. The density waves show only minor reorientations over the time period of several minutes. Scale bars, 50  $\mu\text{m}$ .

of bands or individual clusters or on collision of different actin bands or clusters (Fig. 3). These rotating structures are visible for up to 10 min, after which they dissolve or merge with adjacent and interfering structures. Because all filaments move at the same speed,  $v_0$ , very large gradients of angular velocity are generated throughout a swirl, leading to an inherently metastable structure most often with an unsteady, possibly moving, centre (Fig. 3c and Supplementary Movies 3 and 4).

A key characteristic of pattern-forming systems are their dynamics and stability far from thermal equilibrium. Whereas some systems result in stationary patterns, which do not change their form and structure in time, others may show highly dynamic spatiotemporal patterns. The latter rely on a constant reorganization governed by distinct assembly and disassembly pathways visible in the behaviour of the order parameter. In the high-density motility assay, described here, these reassembly processes result in a characteristic orientational persistence, which increases with increasing filament density. The orientational persistence can directly be related to the underlying disassembly mechanisms using the velocity autocorrelation function,  $G(\tau)$ . For each grid point of a particle image velocimetry sampling

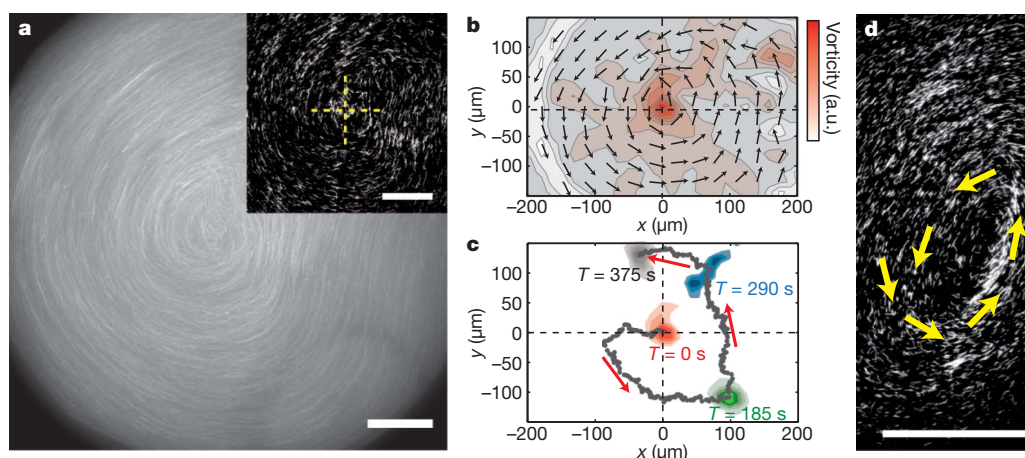


**Figure 3 | Swirling pattern of coherently moving filaments.** a, Swirling motion visualized in a time overlay of ten consecutive images over 1.17 s, starting from the image depicted in the inset. Because all filaments move with the same velocity,  $v_0$ , swirls are characterized by great angular velocity gradients, leading to an inherent destabilization of the pattern. b, c, The resulting unsteady movement can be studied by evaluating the velocity fields and the corresponding vorticity profile (b). The maximum of the vorticity

profile, marking the centre of the anticlockwise-rotating swirls, performs an anticlockwise trajectory (c). In the course of this movement, a deformation of the initially well-defined swirl develops (at  $T = 290 \text{ s}$ ), eventually leading to disintegration of the swirling pattern (Supplementary Movie 3). a.u., arbitrary units. d, The limited stability of swirling motions is visible in the vicinity of the centre region, where crushing of the filament currents is likely to occur (Supplementary Movie 4). Scale bars, 50  $\mu\text{m}$ .

grid (Methods Summary),  $G(\tau)$  reflects local decorrelations assigned to local orientational fluctuations. Averaging over particle image velocimetry grid points for a large sample area results in a spatially averaged autocorrelation function,  $\langle G(\tau) \rangle$ , which characterizes global decorrelations resulting from reorientations of larger areas or destructions of entire clusters or patterns (Supplementary Information and Methods Summary). All decorrelation mechanisms are governed by the persistence of the underlying random walk of the individual filaments and filament–filament interactions. Both processes prevent any instantaneous destruction of patterns.

Above  $\rho_c$ , in the intermediate-density regime,  $\langle G(\tau) \rangle$  decays within seconds (Fig. 4a). The gradual increase of  $\rho$  within this regime results in greater decorrelation times. Small clusters lose their global correlation either because of their limited overall orientational persistence or through large-scale directional changes, such as bending. Bigger clusters frequently show an internal loss of polar nematic order due to gradually developing splay patterns (Fig. 4 and Supplementary Movie 5). Although such internal cluster dynamics lead to a characteristic gradual change in  $G(\tau)$ , spontaneous bending, which is predominantly observed for small clusters, shows rapid and large decorrelations (Fig. 4a). Because these directional instabilities predominantly develop at the margin of moving clusters, the enhanced stability of larger clusters, which have greater area-to-boundary ratios, is intuitive. Consequently, clusters below  $50 \mu\text{m}$  in diameter are unstable as they tend to disintegrate from their margins, and the larger the clusters, the longer they live. At the same time, larger cluster do show a less erratic motion with less frequent reorientations.

In the high-density regime above  $\rho^*$ , the decorrelation time averages up to several minutes, which implies ordered structures spanning length scales of the order of several millimetres. These density waves are only destroyed by global decorrelation mechanisms, such as large-scale reorientations. Provided that structures are more likely to disintegrate from their margins, and owing to the closer packing within the highly ordered and interconnected bands,

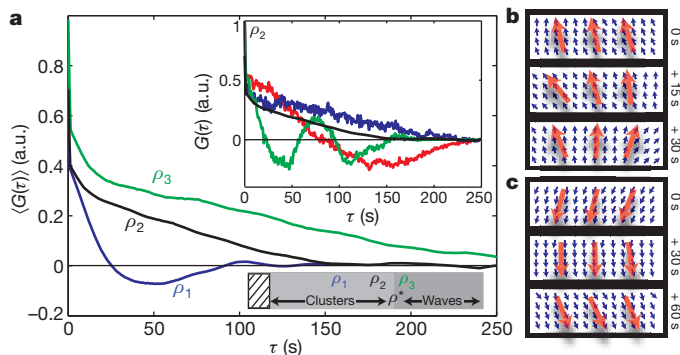


**Figure 4 | Directional persistence and instability mechanisms.** **a**, Spatially averaged autocorrelation functions,  $\langle G(\tau) \rangle$ , for three different densities,  $\rho_1 = 10 \mu\text{m}^{-2}$ ,  $\rho_2 = 18 \mu\text{m}^{-2}$  and  $\rho_3 = 21 \mu\text{m}^{-2}$ . For the intermediate densities,  $\rho_1$  and  $\rho_2$ , homogenous structures are observed;  $\rho_3$  is in the high-density regime immediately above the transition to density waves, at  $\rho^*$  (lower inset). With increasing filament density, the directional persistence of the polar current increases; this is visible in an enhanced correlation time from  $\rho_1$  to  $\rho_2$ . The anticorrelation in the curve for  $\rho_1$  reflects the systematic  $180^\circ$  turns observed at small densities (Fig. 2a, b). Above  $\rho^*$ , the correlation time is of the order of several minutes. Because the emergence of density waves requires a transient of the order of minutes, and because reorientations annihilate density fluctuations, the high directional steadiness found in the high-density regime is the precondition for the emergence of density waves. The local autocorrelation functions,  $G(\tau)$ , depict the underlying decorrelation mechanisms (upper inset). The anticorrelation observed in the red curve reflects a large-scale reorientation of the entire structure by  $180^\circ$ . A splay-like pattern results in a local decorrelation, shown in the blue curve, and oscillatory bending movement results in a local decorrelation, shown in green. a.u., arbitrary units. **b**, **c**, Loss of order through splay (**b**) and bend (**c**) instabilities visualized in the local velocity profiles (Supplementary Movie 5).

density waves are inherently more stable and less prone to bend and splay instabilities or the formation of swirls. Thus, the system self-stabilizes the coherently moving state; in turn, the high decorrelation time is a prerequisite for the emergence of the density wave.

This can be demonstrated by observing the temporal evolution of the underlying density instability. An isotropic and homogenous state, prepared in the absence of ATP, rapidly evolves into a homogeneously moving polar state on addition of ATP. The subsequent emergence of density waves requires a minimal orientational persistence that is only provided by the high densities above  $\rho^*$ . In this regime, local decorrelation mechanisms are not effective enough to result in the destruction or reorientation of the polarity of the entire transient homogenous state. However, they induce persistent density fluctuations that grow gradually in time to form the characteristic density waves. This can be seen in a dynamic Fourier analysis of the density profile in a reference frame along the mean direction of motion. Initially there is a wide band of wavelengths and it takes several minutes for the power spectrum to peak, at about three times the persistence length ( $50 \mu\text{m}$ ; Supplementary Fig. 1).

Along the direction of movement, the density waves are characterized by an abrupt change in the filament density. Whereas the density profile is symmetric, that of the orientational order is asymmetric, with a sharp front edge and a decaying tail (Supplementary Fig. 2b). This is due to the fact that the randomly moving filaments are oriented by the moving bands but cannot immediately adopt this imposed reorientation. In the low-density zone, they gradually lose the directional bias as a result of the randomized movement at low filament densities. As a consequence, they follow a circular trajectory and are eventually overrun by a high-density band (Supplementary Fig. 2c).

This lateral memory effect is intimately related to the persistence of single-filament motion as well as to microscopic interactions between individual filaments, which are short ranged in nature. In low-density motility assays, encounters between filaments most frequently lead to crossing events with only slight reorientations. Rarely, a steric repulsion with an instantaneous and significant directional change of the filaments is observed. Such probabilistic movement of the filaments can readily be modelled using agent-based simulations. The agents are finite-length filaments each performing a persistent random walk and interacting with other filaments through steric repulsion, parameterized by  $\zeta$ , and weak local alignment interactions, measured by a parameter  $\alpha$  (Methods Summary). The simulation is implemented on a hexagonal lattice with reflecting boundary conditions (Fig. 5a) and system sizes large enough to ensure that boundary effects on the emergence of patterns are negligible (Supplementary Movie 7). The symmetry-breaking nature of the local alignment interactions is crucial; without it, filaments interact only sterically and do not show collective motion at all (Fig. 5b). For a fixed parameter set, a small increase in the alignment parameter ( $\alpha > 3.5$ ) drastically changes the outcome, and polar nematic structures developing to wave-like patterns are observed (Fig. 5b–d and Supplementary Movie 6). In contrast, increasing the strength of the steric repulsion, using  $\zeta$ , suppresses the formation of collectively moving polar nematic patterns (Supplementary Fig. 3d). For fixed values of  $\alpha$  and  $\zeta$ , a critical density is required for the polar nematic patterns to form (Supplementary Fig. 3b).

Thus, it is the cooperative effect of many interacting filaments, together with the weak alignment interactions, that leads to the collective order phenomena based on the balanced uptake and loss dynamics of the individual constituents. Purely steric repulsion and high densities do not suffice to induce any order in this system entirely driven by the input of mechanical energy at the smallest scales.

Importantly, the cellular automaton simulations produce very little spontaneous swirling motion. This can be attributed to the lack of weak long-range interactions, such as hydrodynamics, which may be self-induced by the moving clusters. This contribution may turn out to be an important ingredient for the great stability observed in the high-density wave regime. Theoretical approaches best suited for a



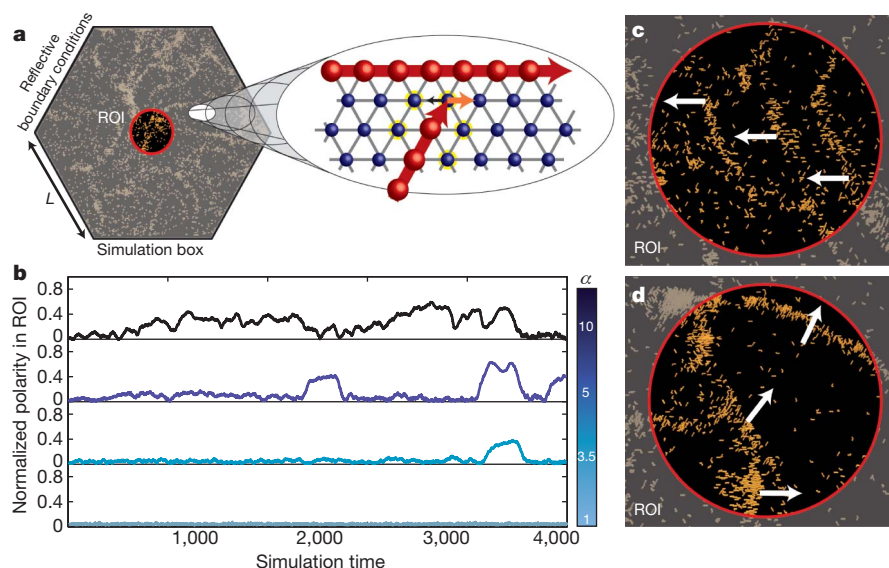


**Figure 5 | Cellular automaton simulations.** **a**, Schematic of the cellular automaton simulations. The persistent random walk and filament–filament encounters are simulated by probabilistic selection rules. They include a weak excluded-volume effect and local alignment interactions, parameterized by  $\alpha$  (orange arrow; Supplementary Information and Methods Summary). Simulations are implemented on a hexagonal lattice and are performed in a hexagonal simulation box with reflective boundary conditions. The total system has a typical length,  $L$ , of 1,000 lattice sites. The filament length is set to 10 lattice sites; their mean density,  $r$ , is measured as a percentage of occupied lattice sites. **b**, Normalized polarity is evaluated in a

region of observation (ROI) with a diameter of  $L/10$ . For small weightings of the alignment interactions,  $\alpha$ , no polar structures form (lowermost curve). Polar-ordered structures start to evolve at  $\alpha = 3.5$  and are visible in the clearly peaked polarity time courses in the upper curves ( $r = 83\%$ ,  $\zeta = 10$ ). **c**, **d**, Distinct peaks reflect the passage of polar nematic structures, either wave-like (**c**; Supplementary Movies 6 and 7) or aggregated (**d**; Supplementary Movies 6 and 7). With increasing  $\alpha$ , an increasing fraction of filaments is recruited to the polar structures; this is visible in a higher overall polarity at earlier simulation times (upper curves in **b**).

description of such phenomena seem to be generic hydrodynamic approaches taking into account the coupling of density fluctuations with solvent dynamics<sup>2,13,25</sup>.

Although the recently introduced theory of active fluids provides a general framework for the investigation of non-equilibrium dynamics driven by local internal forces, a thorough understanding of the underlying mechanism for the emergence of highly ordered structures is still lacking. The combined approach of well-controlled experimental and theoretical model systems described here is ideally suited to identifying the link between microscopic interactions, density and macroscopic structures. The minimal approach and detailed control of all relevant system parameters allows the identification of a remarkable variety of spatiotemporal patterns and permits the backtracking of the assembly and disassembly pathways to the underlying local interactions. By extending the experimental system to include more complex interactions, confined geometries or external stimuli<sup>28</sup>, the mechanically ordered system will become an ideal study tool to accompany theoretical efforts to obtain a sound physical understanding of emerging order in active fluids. The further exploration of this material class will have profound consequences on our understanding of collective effects prominent in diverse fields including cell biology, tissue formation and social systems.

## METHODS SUMMARY

We prepared actin filaments and HMM motor proteins using standardized protocols. The average length of the actin filaments was controlled by adding gelsolin before polymerization. For fluorescence microscopy, fluorescently labelled reporter filaments stabilized with Alexa Fluor 488 phalloidin were used; unlabelled filaments were stabilized with phalloidin. We prepared actin dilutions (5–25  $\mu\text{M}$  monomeric actin) by gently mixing labelled and unlabelled actin filaments at a ratio of 1:200 to 1:320. Flow chambers were prepared with nitrocellulose-coated coverslips. After the incubation with HMM, surfaces were first passivated using BSA and then the prepared actin dilution was inserted. Then filaments not bound to motor proteins were flushed out by a second rinse with BSA solution. To start the experiment, we added 4  $\mu\text{M}$  ATP. Oxidation of the fluorophore was prevented by adding a standard antioxidant buffer supplement.

The presented velocity fields were calculated with a particle image velocity algorithm. We evaluated the autocorrelation function of the velocity field,  $v$ , according to

$$G(\tau) = \frac{\langle v(t+\tau)v(t) \rangle - \langle v(t) \rangle^2}{\langle v(t)^2 \rangle - \langle v(t) \rangle^2}$$

where angle brackets denote the time average. It provides information about local decorrelations. The spatially averaged correlation function,  $\langle G \rangle$ , averaged over all accessible velocity vectors, shows the global behaviour of the correlation function.

We implemented cellular automaton simulations on a hexagonal lattice with a side length of 1,000 lattice sites. Each of the five degrees of freedom of each filament head was weighted by a certain probability,  $P$ , yielding a persistent random walk for a single filament. These probabilities were modified by filament–filament interactions. Steric contributions were weighted by the steric repulsion parameter,  $\zeta$ , and the strength of local alignment was measured with a local alignment parameter,  $\alpha$ . For the data presented, reflecting boundary conditions were used and the filament length was adjusted to 10 lattice sites.

Received 23 February; accepted 24 June 2010.

- Karsenti, E. Self-organization in cell biology: a brief history. *Nature Rev. Mol. Cell Biol.* **9**, 255–262 (2008).
- Kruse, K., Joanny, J. F., Jülicher, F., Prost, J. & Sekimoto, K. Asters, vortices, and rotating spirals in active gels of polar filaments. *Phys. Rev. Lett.* **92**, 078101 (2004).
- Loose, M., Fischer-Friedrich, E., Ries, J., Kruse, K. & Schwiile, P. Spatial regulators for bacterial cell division self-organize into surface waves *in vitro*. *Science* **320**, 789–792 (2008).
- Couzin, I. D., Krause, J., Franks, N. R. & Levin, S. A. Effective leadership and decision-making in animal groups on the move. *Nature* **433**, 513–516 (2005).
- Dombrowski, C., Cisneros, L., Chatkaew, S., Goldstein, R. E. & Kessler, J. O. Self-concentration and large-scale coherence in bacterial dynamics. *Phys. Rev. Lett.* **93**, 098103 (2004).
- Riedel, I. H., Kruse, K. & Howard, J. A. Self-organized vortex array of hydrodynamically entrained sperm cells. *Science* **309**, 300–303 (2005).
- Nedelec, F. J., Surrey, T., Maggs, A. C. & Leibler, S. Self-organization of microtubules and motors. *Nature* **389**, 305–308 (1997).
- Narayan, V., Ramaswamy, S. & Menon, N. Long-lived giant number fluctuations in a swarming granular nematic. *Science* **317**, 105–108 (2007).
- Backouche, F., Haviv, L., Groszasser, D. & Bernheim-Groszasser, A. Active gels: dynamics of patterning and self-organization. *Phys. Biol.* **3**, 264–273 (2006).
- Grossman, D., Aranson, I. S. & Ben Jacob, E. Emergence of agent swarm migration and vortex formation through inelastic collisions. *New J. Phys.* **10**, 023036 (2008).

11. Czirok, A., BenJacob, E., Cohen, I. & Vicsek, T. Formation of complex bacterial colonies via self-generated vortices. *Phys. Rev. E* **54**, 1791–1801 (1996).
12. Surrey, T., Nedelec, F., Leibler, S. & Karsenti, E. Physical properties determining self-organization of motors and microtubules. *Science* **292**, 1167–1171 (2001).
13. Toner, J., Tu, Y. H. & Ramaswamy, S. Hydrodynamics and phases of flocks. *Ann. Phys.* **318**, 170–244 (2005).
14. Baskaran, A. & Marchetti, M. C. Enhanced diffusion and ordering of self-propelled rods. *Phys. Rev. Lett.* **101**, 268101 (2008).
15. Baskaran, A. & Marchetti, M. C. Hydrodynamics of self-propelled hard rods. *Phys. Rev. E* **77**, 011920 (2008).
16. Mishra, S., Baskaran, A. & Marchetti, M. C. Fluctuations and pattern formation in self-propelled particles. *Phys. Rev. E* **81**, 061916 (2010).
17. Vicsek, T., Czirok, A., BenJacob, E., Cohen, I. & Shochet, O. Novel type of phase transition in a system of self-driven particles. *Phys. Rev. Lett.* **75**, 1226–1229 (1995).
18. Chate, H., Ginelli, F., Gregoire, G. & Raynaud, F. Collective motion of self-propelled particles interacting without cohesion. *Phys. Rev. E* **77**, 046113 (2008).
19. Ginelli, F., Peruani, F., Bär, M. & Chaté, H. Large-scale collective properties of self-propelled rods. *Phys. Rev. Lett.* **104**, 184502 (2010).
20. Kraikivski, P., Lipowsky, R. & Kierfeld, J. Enhanced ordering of interacting filaments by molecular motors. *Phys. Rev. Lett.* **96**, 258103 (2006).
21. Aranson, I. S. & Tsimring, L. S. Pattern formation of microtubules and motors: inelastic interaction of polar rods. *Phys. Rev. E* **71**, 050901 (2005).
22. Joanny, J. F., Jülicher, F., Kruse, K. & Prost, J. Hydrodynamic theory for multi-component active polar gels. *New J. Phys.* **9**, 422 (2007).
23. Jülicher, F., Kruse, K., Prost, J. & Joanny, J. F. Active behavior of the cytoskeleton. *Phys. Rep.* **449**, 3–28 (2007).
24. Simha, R. A. & Ramaswamy, S. Hydrodynamic fluctuations and instabilities in ordered suspensions of self-propelled particles. *Phys. Rev. Lett.* **89**, 058101 (2002).
25. Baskaran, A. & Marchetti, M. C. Statistical mechanics and hydrodynamics of bacterial suspensions. *Proc. Natl Acad. Sci. USA* **106**, 15567–15572 (2009).
26. Sheetz, M. P., Chasan, R. & Spudich, J. A. ATP-dependent movement of myosin *in vitro*: characterization of a quantitative assay. *J. Cell Biol.* **99**, 1867–1871 (1984).
27. Fulga, F. & Nicolau, D. V. Models of protein linear molecular motors for dynamic nanodevices. *Integ. Biol.* **1**, 150–169 (2009).
28. van den Heuvel, M. G. L. & Dekker, C. Motor proteins at work for nanotechnology. *Science* **317**, 333–336 (2007).

**Supplementary Information** is linked to the online version of the paper at [www.nature.com/nature](http://www.nature.com/nature).

**Acknowledgements** We thank A. Baskaran and C. Marchetti for discussions. Financial support from the DFG in the framework of the SFB 863 and the German Excellence Initiatives via the 'Nano-Initiative Munich (NIM)' and the Technische Universität München - Institute for Advanced Study is gratefully acknowledged. V.S. and C.W. acknowledge support from the Elite Network of Bavaria by the graduate programmes Complint and NanoBioTechnology.

**Author Contributions** A.R.B., C.S. and V.S. conceived and performed the experiments. C.W. and E.F. conceived and designed the simulations. C.W. performed and analysed the simulations. A.R.B., C.S., V.S., C.W. and E.F. interpreted the data. A.R.B., V.S., C.W. and E.F. wrote the paper.

**Author Information** Reprints and permissions information is available at [www.nature.com/reprints](http://www.nature.com/reprints). The authors declare no competing financial interests. Readers are welcome to comment on the online version of this article at [www.nature.com/nature](http://www.nature.com/nature). Correspondence and requests for materials should be addressed to A.R.B. ([abausch@ph.tum.de](mailto:abausch@ph.tum.de)).